

Article

Effect of Carbon Content on the Phase Composition, Microstructure and Mechanical Properties of the TiC Layer Formed in Hot-Pressed Titanium-Steel Composites

Marius Grad ^{1,2,3,*} , Jan Zentgraf ¹ , Ulrich Schultheiss ¹, Lukas Esper ^{1,3} , Andreas Diemar ^{2,4}, Ulf Noster ^{1,3}  and Lothar Spiess ² 

¹ Department of Mechanical Engineering, University of Applied Sciences Regensburg, 93053 Regensburg, Germany; jan.zentgraf@oth-regensburg.de (J.Z.); ulrich.schultheiss@oth-regensburg.de (U.S.); lukas.esper@oth-regensburg.de (L.E.); ulf.noster@oth-regensburg.de (U.N.)

² Institute of Micro and Nanotechnologies MacroNano[®], Technical University Ilmenau, 98693 Ilmenau, Germany; andreas.diemar@mfpa.de (A.D.); lothar.spieess@tu-ilmenau.de (L.S.)

³ Technology Campus Parsberg-Lupburg, University of Applied Sciences Regensburg, 92331 Parsberg, Germany

⁴ Materials Research and Testing Institute, Bauhaus-Universität Weimar, 99423 Weimar, Germany

* Correspondence: marius.grad@oth-regensburg.de

Abstract: During the hot pressing of pure titanium and different carbon steels in a temperature range of $\theta = 950\text{--}1050\text{ }^{\circ}\text{C}$, a compound layer up to $d_L \approx 10\text{ }\mu\text{m}$ thick is formed at the titanium–steel interface. With a higher carbon content of the used steel, the layer thickness increases. The carbon concentration within the layer is in the range of stoichiometry for TiC. Apart from TiC, no other phases can be detected by X-ray diffraction (XRD) measurements inside the formed layer. The calculation of the activation energy for the TiC layer formation is $Q = 126.5\text{--}136.7\text{ kJ mol}^{-1}$ and is independent of the carbon content of the steel. The resulting microstructure has a grain size gradient, wherein the mechanical properties, such as hardness and Young’s modulus, are almost constant. Statistical analysis using Response Surface Methodology (RSM) indicates that the carbon content of the steel has the most significant influence on layer thickness, followed by annealing temperature and annealing time. By selecting the appropriate carbon steel and the subsequent removal of the steel, it is possible to produce targeted TiC layers on titanium substrates, which holds enormous potential for this material in wear-intensive applications.

Keywords: TiC; hot pressing; layer growth kinetics; electron backscatter diffraction; X-ray diffraction; glow discharge optical emission spectroscopy; nanoindentation



Citation: Grad, M.; Zentgraf, J.; Schultheiss, U.; Esper, L.; Diemar, A.; Noster, U.; Spiess, L. Effect of Carbon Content on the Phase Composition, Microstructure and Mechanical Properties of the TiC Layer Formed in Hot-Pressed Titanium-Steel Composites. *Metals* **2024**, *14*, 959. <https://doi.org/10.3390/met14090959>

Academic Editor: Hongzhi Niu

Received: 31 July 2024

Revised: 19 August 2024

Accepted: 22 August 2024

Published: 24 August 2024



Copyright: © 2024 by the authors. Licensee MDPI, Basel, Switzerland. This article is an open access article distributed under the terms and conditions of the Creative Commons Attribution (CC BY) license (<https://creativecommons.org/licenses/by/4.0/>).

1. Introduction

Titanium and its alloys are widely used due to their excellent strength-to-weight ratio and high corrosion resistance. In addition to their suitability for aerospace, military, microelectronics, and chemical engineering applications, titanium and its alloys are also utilized as implant materials in medicine because of their outstanding biocompatibility [1,2]. However, their performance in high-friction loading applications is limited by low surface hardness and poor wear properties [3].

Various surface treatments have been explored for enhancing the tribological properties of titanium and its alloys. Surface modification techniques, such as physical deposition methods like ion implantation and plasma spray layer, as well as thermochemical surface treatments, like nitriding and carburization, have been utilized to improve the surface hardness of titanium alloys [4]. In these cases, small atoms like C or N diffuse into the surface, forming intermetallic phases or non-stoichiometric structures [5] once their solubility in

titanium is exceeded. These atoms can be introduced by a solid-state diffusion process such as diffusion bonding or hot pressing.

Hot pressing is a process where two substrates are pressed together and heated to a specified temperature for a certain period of time. During this process, different elements can diffuse into the titanium substrate, forming intermetallic phases. When carbon steel is used, C atoms, due to their smaller atomic radius, diffuse more rapidly than other atoms. Given the low solubility of C in Ti, approximately 1.6 at.-% in α -Ti and 0.6 at.-% in β -Ti, titanium carbide particles form almost immediately [6]. The growth and bonding of these TiC particles result in the formation of a continuous TiC layer at the titanium–steel interface. By subsequently removing the carbon steel and exposing the TiC surface, hot pressing demonstrates significant potential as a method for producing a hard TiC layer on the surface of titanium and its alloys [7].

Li et al. [8] investigated the effect of grain orientation on the growth of compounds at the diffusion-bonded titanium–steel interface using medium-carbon steel (MC-Steel, 0.45 wt.-% C). At moderate temperatures (up to $\vartheta = 850^\circ\text{C}$), a maximum layer thickness of about $d_L = 1.6\ \mu\text{m}$ has been achieved after a holding time of $t_h = 16\ \text{h}$. Zhao et al. [9] achieved a TiC layer thickness of up to $23\ \mu\text{m}$ using nodular cast iron (3.7 wt.-% C) as a carbon source. In a preliminary study, a graded microstructure was observed using EBSD analysis [10].

Yu et al. [11] investigated the influence of carbon content on the diffusion bonding of steel to titanium. They found that the layer at the interface increases with a higher carbon content of the steel. Using low-carbon steel (LC-Steel, 0.14 wt.-% C), the layer formed included TiC, FeTi, and Fe₂Ti. In contrast, when medium-carbon steel (MC-Steel, 0.43 wt.-% C) was used, only TiC was detected. In addition, Momono et al. [12] were also able to show that the use of cast iron prevents the formation of Fe-Ti compounds. The complete formation of the TiC layer effectively prevented the diffusion of Fe and Ti, thereby inhibiting the further formation of Fe-Ti compounds. These experiments demonstrate the potential for creating a TiC layer at the titanium–steel interface by hot pressing.

Zhao et al. [7] conducted a study examining the influence of the carbon source by utilizing both gray cast iron and bulk graphite. However, they were only able to generate a non-uniform and porous layer with significantly lower hardness, measuring $900\ \text{HV}_{0.05}$, when bulk graphite was used as carbon source, compared to $2400\ \text{HV}_{0.05}$ when gray cast iron was used. Similarly, Hayashi et al. [13] reported the formation of TiC layers on titanium through heat treatment with graphite powders using the spark plasma sintering method. The difference between the results shown previously relates to the bonding of the carbon atoms. In steel, the carbon is available as an interstitial atom, whereas, in bulk graphite, it is found in C-C bonds. This C-C bond must be broken before diffusion. As soon as this bonding is broken, carbon is available in high concentrations, which leads to a violent reaction with Ti, resulting in a porous layer [14]. Porous layers resulting from this violent reaction have been observed in various studies [15,16]. This porous structure is the cause of poor layer adhesion or spalling observed in these experiments. Another reason for achieving a slow diffusion is the change in volume caused by the formation of TiC. The reaction of two elementary cells of titanium (four atoms Ti) with one elementary cell of graphite (four atoms C) produces one elementary cell of TiC, containing four compounds TiC. The difference between the theoretical and real unit cell size leads to a volume shrinkage of 23.5%. This can be shown by the elementary cell equation [10]. This change in volume can lead to defects in the layer. With slow diffusion, the resulting stresses are less likely to occur. By selecting different steels with different carbon concentrations, the carbon available for TiC formation can be limited. A local layer can also be applied due to the local contact between steel and titanium.

These experiments demonstrate the potential for producing a TiC layer at the titanium–steel interface by hot pressing. However, the influence of the carbon content in hypereutectoid and hypoeutectoid steels as starting material for hot pressing and the direct influence on the layer formation are not sufficiently described. Therefore, it is important to ensure

that carbon is dissolved interstitially and the steel contains almost no other alloying elements that could hinder the diffusion of carbon. The aim of this study is to investigate the influence of carbon content on the layer growth, the microstructure, the phase composition, and the mechanical properties of the formed layer at the titanium–steel interface during hot pressing. In a temperature range of $\vartheta = 950\text{--}1050\text{ }^{\circ}\text{C}$ (Ti only containing β -phase and steel only containing γ -phase), the influence of carbon content is determined using optical light microscopy, electron backscatter diffraction (EBSD), glow discharge optical emission spectroscopy (GDOES), X-ray diffraction (XRD), and nanoindentation. A detailed material analysis is carried out on the titanium–steel interface layer produced by hot pressing using a number of different carbon steels as starting materials.

2. Materials and Methods

Pure titanium grade 2 and carbon steels with different compositions were utilized as starting materials. The chemical compositions can be seen in Table 1. The size of the samples was $10 \times 15\text{ mm}$ with a thickness of 2 mm. The interfaces of the samples were ground up to 2500# SiC abrasive paper and subsequently cleaned in ethanol. The specimens were pressed together using a clamping device [10], achieving an initial pressure of 50 MPa. This pressure was intended solely for initial contact. The pressure drops to a minimum of less than 1 MPa during the process, preventing a plastic deformation due to creep during annealing [17]. He et al. [18] have demonstrated in their studies that contact pressure does not affect the layer thickness. The specimens were then annealed at different temperatures ($\vartheta = 950\text{--}1050\text{ }^{\circ}\text{C}$) with a heating rate of 20 K min^{-1} . To prevent oxidation, inert argon gas (purity 4.6) was used. After a varying 2–8 h holding period, the samples were cooled to room temperature in the furnace within approx. 1.5 h. For metallographic analysis, a multi-step etching process was performed to detect different sections [10]. In order to determine the influence of the individual process parameters (annealing time, annealing temperature, and carbon content) on layer formation, an analysis of variance (ANOVA) of the response surface methodology (RSM) experimental design is used. As the normal distribution (Anderson–Darling Test) of the residuals and the equality of the variances (Bartlett’s Test) are essential conditions for the interpretation [19], these are also checked as part of the ANOVA. The analysis of the data is carried out using the software Minitab 18 (Minitab. Inc., PA, USA).

Table 1. Chemical composition of the raw materials in wt.-%.

Materials	C	Mn	Si	P	S	Cr	Ni	Mo	O	N	Ti	Fe
MC-Steel 1	0.454	0.732	0.236	0.038	0.038	0.026	0.016	0.002	-	-	-	Bal.
MC-Steel 2	0.673	0.663	0.245	0.016	0.017	0.183	0.038	0.005	-	-	-	Bal.
HC-Steel	0.993	0.463	0.259	0.015	0.021	0.203	0.039	0.023	-	-	-	Bal.
UHC-Steel	1.153	0.611	0.091	0.015	0.002	0.088	0.012	0.011	-	-	-	Bal.
Ti cp.2	0.059	-	-	-	-	-	-	-	0.09	0.03	Bal.	0.1

A Bruker Davinci diffractometer, Cu-K α radiation, in Bragg–Brentano arrangement with variable optics and semiconductor strip detector LynXEye with 192 lines and goniometer radius $r = 420\text{ mm}$, was used. In the case of the semiconductor detector, the use of a metal filter is not necessary because of the high energy discrimination of $E = 380\text{ eV}$. In order to keep the irradiated areas relatively small, a 1 mm double aperture (snout) was used. Diffractograms were analyzed using Bruker’s Diffrac-Eva V5.2 software and ICCD’s PDF4 file [20,21]. For the X-ray analysis, the carbon steel must be removed. Therefore, the sample was exposed to citric acid (40%) at $\vartheta = 60\text{ }^{\circ}\text{C}$. An iron citrate complex is formed between the iron and the citric acid, resulting in the complete removal of the steel while the titanium remains undissolved. The chemical resistance of titanium against citric acid is well-documented, with a corrosion rate (cr) less than $cr = 0.01\text{ mpy}$ [22]. The exposed TiC layer is defect-free with a mean surface roughness value of $S_a = 0.15\text{ }\mu\text{m}$, as proven by laser scanning microscopy.

The GDOES investigations were carried out with a GDA 750 spectrometer from Spectrum Analytik. This spectrometer is equipped with a glow discharge source, whose geometry is based on a measuring arrangement according to Grimm [23]. The cathode diameter is $\varnothing = 2.5$ mm. The depth profiles were measured in direct current (DC) mode. For the measurements, different photomultipliers with varying transmission properties in the window were used due to the different wavelengths of the emission lines. The process parameters were $U = 1200$ V and $I = 13$ mA [10].

A Tescan Mira field emission scanning electron microscope (SEM) was used to perform the microstructure analysis. Therefore the cross-sections were ground up to 2500# SiC abrasive paper and final polished with colloidal silica ($0.03 \mu\text{m}$). Grain orientation and texture were determined via the EBSD technique using a Velocity Pro detector from EDAX AMETEK. The SEM operated at $U = 20$ keV and $I = 1$ nA current during EBSD analysis, with a sample tilt angle of 70° and a working distance of $WD = 15$ mm. For TiC, the structure data from the ICDD's PDF4 database (PDF 00-032-1383) were used for pattern identification and indexing in EBSD measurements and evaluation. EBSD raw data were processed using commercially available ATEX software (<http://www.atex-software.eu/>) [24]. For EBSD cleanup, a grain dilation with a minimum grain area of 10 points and a grain tolerance angle of 5° was performed. Finally, with a grain size filter (tolerance angle 5°), all grains smaller than 5 points were removed.

Nanoindentation experiments were performed in situ using a NanoFlip InForce 50 nanoindenter (Nanomechanics Inc., Oak Ridge, TN, USA). The objective of the nanoindentation testing was to evaluate the hardness, Young's modulus, and plasticity of the formed TiC layer. A Berkovich-type indentation tip was used for the testing. The entire nanoindentation setup was assembled inside the TESCAN Clara SEM prior to testing. Prior to the indentation experiment, a thermal drift rate below 0.010 nm s^{-1} was set to allow thermal equilibrium between the sample and the indenter. Given that the tip is diamond with a Young's modulus $E_i = 1050$ GPa and Poisson's ratio $\nu_i = 0.104$, the Young's modulus E of titanium carbide can be calculated via the Oliver–Pharr method [25] using $\nu = 0.185$ for titanium carbide [26,27]. In addition to hardness and Young's modulus, the percentage of elastic recovery during unloading is determined. This is calculated using the ratio of elastic deformation to the maximum penetration depth of the indenter [28–31]. Single and multiple indentation tests were performed within the TiC layer using a maximum force of $F = 50$ mN and a constant strain rate of $\epsilon = 0.002 \text{ s}^{-1}$. The measurement data were evaluated using the InView Review Data software 1.1. The Nanoblitz 3D method available in the InView software was used for the indentation mapping.

3. Results and Discussion

Optical microscope (OM) images show the growth of the compound layer close to the titanium–steel interface (see Figure 1). This layer was produced using an annealing time of $t_h = 4$ h and a process temperature of $\vartheta = 1000$ °C. It is noticeable that the layer thickness increases as the carbon content of the applied steel becomes higher, which has also been proven by Momono et al. [12] using stainless steel and cast iron. As the carbon concentration increases, the carbon atoms can diffuse into the titanium substrate more rapidly as a result of a higher concentration gradient, and a TiC layer forms immediately due to the low solubility of C in β -Ti [12]. The layer thickness is $d_L = (3.36 \pm 0.22) \mu\text{m}$ when using the MC-Steel 1 and increases to $d_L = (7.04 \pm 0.28) \mu\text{m}$ when using the UHC-Steel. After applying Groesbeck etchant, an area of the layer can be etched. This etched layer also increases with carbon content.

During the diffusion process, the growth of the compound layer is proportional to the square root of the diffusion time t_h at constant temperature T ,

$$d_L = \sqrt{K \cdot t_h} \quad | T = \text{const.} \quad (1)$$

where d_L is the TiC layer thickness and K is the growth rate constant. Figure 2a indicates the linear relationship between layer thickness d_L and the square root of time t_h (parabolic

relation) at an annealing temperature $\vartheta = 1050^\circ\text{C}$. When using UHC-Steel, a maximum thickness of $d_L = (9.56 \pm 0.19) \mu\text{m}$ can be achieved. The positive correlation between the carbon content of the steel and the layer thickness can also be seen in Figure 2a.

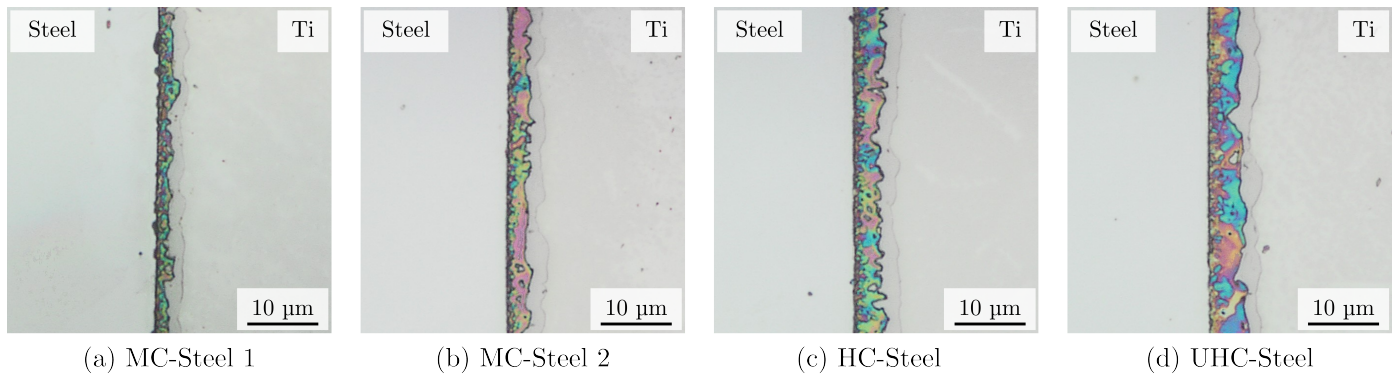


Figure 1. OM images of the diffusion layer at the titanium–steel interface when using various carbon steels with different carbon contents (Table 1). Parameters for process temperature and annealing time are $\vartheta = 1000^\circ\text{C}$ and $t_h = 4 \text{ h}$, respectively.

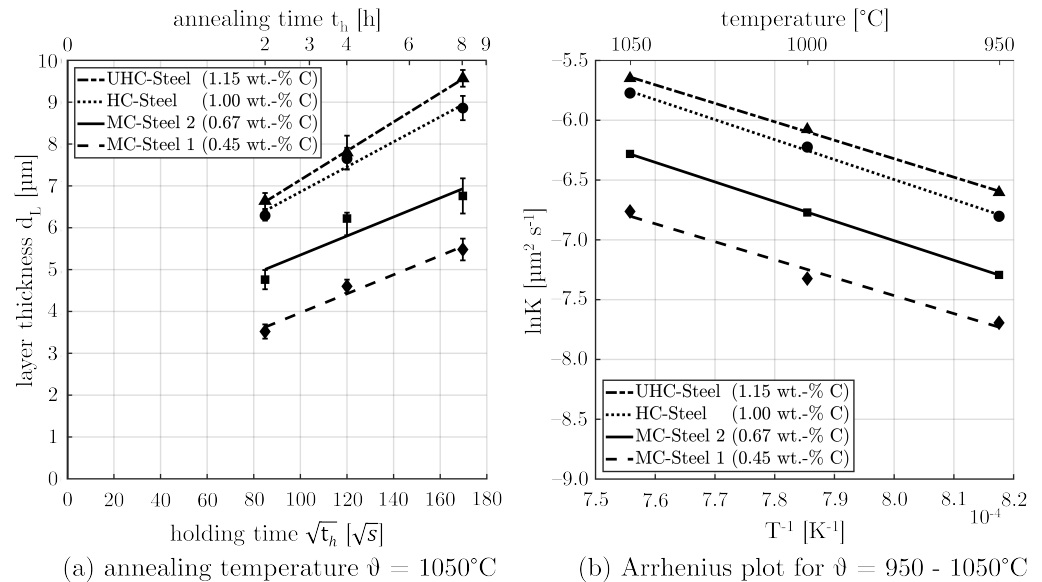


Figure 2. (a) Relationship between layer thickness d_L and annealing time t_h when using different carbon steels and (b) Arrhenius correlation $\ln K$ vs. T^{-1} .

The growth rate constant can be determined by the slope of the linear regression. As the slope of the regression increases with increasing carbon content, the growth rate constant also increases with higher carbon content. The growth factors are summarized in Table 2. The growth rate constant is a temperature-dependent value following the Arrhenius relationship [18,32]:

$$K = K_0 \cdot e^{\frac{-Q}{R \cdot T}} \quad (2)$$

The growth rate constant can be determined using Equation (2), where K_0 is a pre-exponential constant, Q is the activation energy for layer growth, R is the gas constant, and T is the annealing temperature in Kelvin. Plots of $\ln K$ vs. T^{-1} are represented in Figure 2b for the different carbon steels used. By analyzing the slope of the linear relationship between $\ln K$ and T^{-1} , the activation energy of the process can be determined. The activation energy varies between $Q = 126.5$ and $136.7 \text{ kJ mol}^{-1}$, independently of the carbon content of the carbon steel. This energy directly refers to the interaction of carbon and titanium

atoms for the formation of the TiC layer. Arvieu et al. [33] determined an activation energy of TiC layer growth of $Q = (153 \pm 18) \text{ kJ mol}^{-1}$ using a sputter process at moderate temperatures up to $650 \text{ }^\circ\text{C}$, referring to the activation energy for the diffusion of C in Ti ($Q = 130\text{--}180 \text{ kJ mol}^{-1}$) [34]. The value of the activation energy determined in the current study agrees well with the value of $Q = 109 \text{ kJ mol}^{-1}$ determined by Capaldi et al. [35], which corresponds to the dissolution of carbon in molten titanium ($Q = 117 \text{ kJ mol}^{-1}$). Feng et al. [36] calculated a value of $Q = 87 \text{ kJ mol}^{-1}$ using a carburizing agent containing barium carbonate, calcium carbonate, and charcoal powder.

Table 2. Growth rate constant K in $[\mu\text{m}^2 \text{ s}^{-1}]$ and activation energy Q in $[\text{kJ mol}^{-1}]$ for the growth of the compound layer for the different carbon steels used

	MC-Steel 1 0.45 wt.-% C	MC-Steel 2 0.67 wt.-% C	HC-Steel 1.00 wt.-% C	UHC-Steel 1.15 wt.-% C
K at $\vartheta = 950 \text{ }^\circ\text{C}$	4.78×10^{-4}	6.58×10^{-4}	1.11×10^{-3}	1.37×10^{-3}
K at $\vartheta = 1000 \text{ }^\circ\text{C}$	8.14×10^{-4}	1.08×10^{-3}	1.93×10^{-3}	2.16×10^{-3}
K at $\vartheta = 1050 \text{ }^\circ\text{C}$	1.23×10^{-3}	1.76×10^{-3}	3.06×10^{-3}	3.50×10^{-3}
Q	127.0	132.5	136.7	126.5

Figure 3 presents contour plots representing the layer thickness as a function of annealing temperature and annealing time. The isometric lines correlate with a certain layer thickness. It can be seen that the maximum layer thickness is reached in the top right-hand corner (maximum time and maximum temperature). The isometric lines tend to shift from the top-right corner to the bottom-left corner as the carbon content increases.

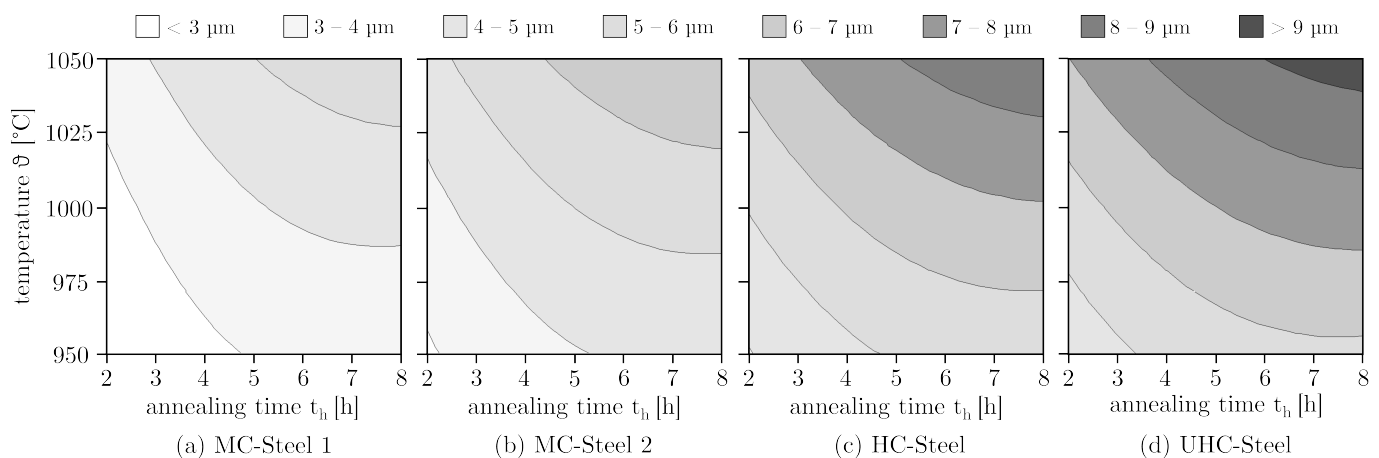


Figure 3. Contour plot for layer thickness vs. temperature ϑ and annealing time t_h for the different carbon steels investigated.

The analysis of variance (Table A1) of the RSM model resulted in the carbon content as well as the annealing temperature and annealing time having a significant influence on the layer thickness. The mean layer thickness can be calculated using

$$\begin{aligned}
 d_L [\mu\text{m}] = & + 28.7 \\
 & - 11.12 \cdot A - 0.0629 \cdot B - 0.951 \cdot C \\
 & - 1.121 \cdot A^2 + 0.000033 \cdot B^2 - 0.0494 \cdot C^2 \\
 & + 0.01692 \cdot AB + 0.001687 \cdot BC + 0.072 \cdot CA
 \end{aligned} \tag{3}$$

where A equals the carbon content of the steel, B equals the annealing temperature, and C equals the annealing time. The regression analysis ($R^2 = 0.983$) is only valid in the

intervals $A \in [0.45, 1.15]$, $B \in [950, 1050]$, and $C \in [2, 8]$. To determine the influence of an isolated parameter, the standardized effect of a particular parameter on the layer thickness is shown in Figure 4. In addition to the influence of single parameters, interactions and squared effects can also be interpreted [37]. If this standardized effect is higher than 2.06, it represents a significant ($\alpha = 0.05$) influence. The squared carbon content, the squared annealing temperature, and the product of carbon content and annealing time have no significant influence. All other combinations are significant. The carbon content has the greatest influence, followed by the annealing temperature and the annealing time.

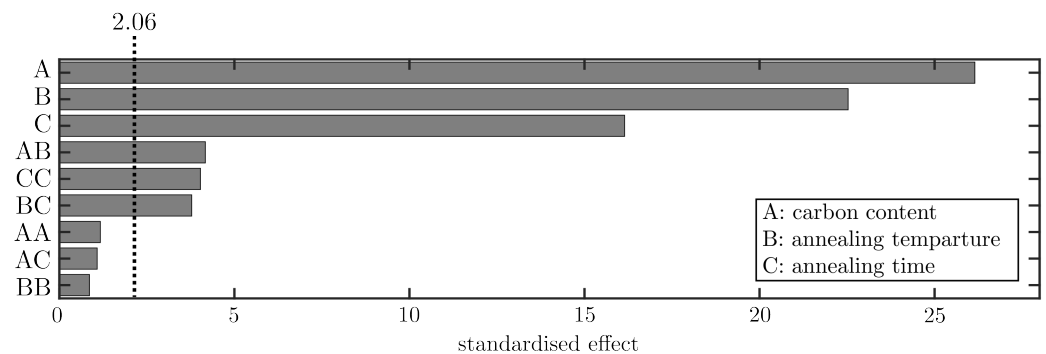


Figure 4. Pareto chart of the standardized effect corresponding to the response: layer thickness (confidence interval $\alpha = 0.05$).

Figure 5 shows the determined element depth profiles for Ti and C using different carbon steels as starting materials for hot pressing. A maximum concentration of approx. 23 wt.-% is observed in all investigated variants. The higher the carbon concentration of the carbon steel, the longer the depth profile remains at this maximum. In addition, the range of stoichiometry for TiC is given and, as soon as the concentration is below the minimum of the range of stoichiometry (at approx. 10.5 wt.-%), a substoichiometric composition of TiC is present, which cannot be etched by Groesbeck etching agent [38,39]. By using a steel with a higher carbon concentration, the depth profile for carbon is shifted to greater depths. For example, the carburization depth for 10.5 wt.-% C when using MC-Steel 1 is 2.07 μm , for MC-Steel 2 is 2.83 μm , for HC-Steel is 3.94 μm , and for UHC-Steel is increased to 4.72 μm . The effect of the process on the concentration of certain other elements, such as oxygen or nitrogen, can be excluded after taking reference samples. The element Fe could not be detected in any of the examined variants, which proves that the chemical removal by citric acid has completely dissolved the carbon steels. This also prevents the formation of other phases like Fe_2Ti or FeTi . These phases are detected in numerous other studies [40–43]. These investigations mostly use stainless steels as starting materials for hot pressing. The carbon content of stainless steel is not sufficient to form an initial TiC at the interface, which acts as a barrier for the diffusion of other elements [12,44]. In the Fe-Ti-C system, TiC (-42 kJ mol^{-1}) has the lowest free energy of formation compared to Fe_2Ti (-19 kJ mol^{-1}) and FeTi (-8 kJ mol^{-1}), making it the dominant phase at the interface [43,45].

The X-ray diffractograms, seen in Figure 6, prove that no intermetallic Fe-Ti compounds can be detected inside the layer. Only the α -Ti and TiC phases can be found. While TiC shows a simple NaCl crystal structure, Fe_2Ti and FeTi have more complex structures. Fe_2Ti is MgZn_2 -type and FeTi is bcc- or CsCl-type. Fe_2Ti is known as a Laves phase, which is hard but very brittle. Considering the crystal structures of these phases, it seems unlikely that TiC is as brittle as FeTi and Fe_2Ti [12]. Thus, it is important to ensure that no Fe-Ti compounds are formed at the interface during the process. As shown in studies by Yu et al. [46], intermetallic Fe-Ti compounds can only be detected at higher temperatures ($>1000 \text{ }^\circ\text{C}$). Their study used LC-Steel (0.15 wt.-% C) and Ti6Al4V for hot rolling. At low temperatures, the thin TiC layer acts as a barrier to the diffusion of elements such as Fe, Ti, Al, or V. This prevents the formation of other phases. By increasing the temperature, the barrier effect of the TiC layer is overcome and Fe diffuses due to the highest concentration

and forms intermetallic compounds with titanium. By using a ferritic spheroidal graphite cast iron (3.75 wt.-% C), Momono et. al. [12] were able to show that the formation of Fe-Ti compounds can also be prevented at higher temperatures of $\vartheta = 1000\text{ }^{\circ}\text{C}$. Yu et al. [11] found similar results in their investigations on the influence of the carbon content on the bonding properties of Ti–steel composites. When LC-Steel (0.14 wt.-% C) is used, the formation of Fe-Ti compounds at $\vartheta = 1050\text{ }^{\circ}\text{C}$ cannot be avoided. The use of MC-Steel (0.43 wt.-% C) leads to a stable TiC layer after a short time, and Fe-Ti compounds can no longer be found. According to Bene and Walser’s rule, the phase closest to the lowest eutectic temperature predominantly forms. However, reaching the eutectic temperature is not a prerequisite for the formation of this phase [47]. The eutectic temperature of Fe-Ti compounds is $\vartheta = 1085\text{ }^{\circ}\text{C}$ for FeTi and $\vartheta = 1289\text{ }^{\circ}\text{C}$ for Fe₂Ti [48], which are significantly lower than $\vartheta = 2776\text{ }^{\circ}\text{C}$ for TiC [49,50], but carbon diffuses faster than iron into the titanium substrate due to the smaller atomic radius and, therefore, also forms a TiC layer due to the lower free energy, which prevents the diffusion of other atoms. The diffusion coefficients in α -Ti for carbon and iron at approx. $900\text{ }^{\circ}\text{C}$ are $D_{\text{C}}(\alpha\text{-Ti}) = 5.9 \times 10^{-10}\text{ m}^2\text{ s}^{-1}$ and $D_{\text{Fe}}(\alpha\text{-Ti}) = 7.0 \times 10^{-13}\text{ m}^2\text{ s}^{-1}$ [51]. Due to the high range of stoichiometry for TiC and the resulting high vacancy density, further C atoms can diffuse through the TiC layer and react with the basic substrate titanium. The higher the carbon content of the steel, the lower the intensity of the α -Ti peaks. The diffraction peaks of the β -Ti phase were not found. The α -Ti peak at $2\theta = 40.171^{\circ}$ relates to the (101) reflex and can be detected in all variants.

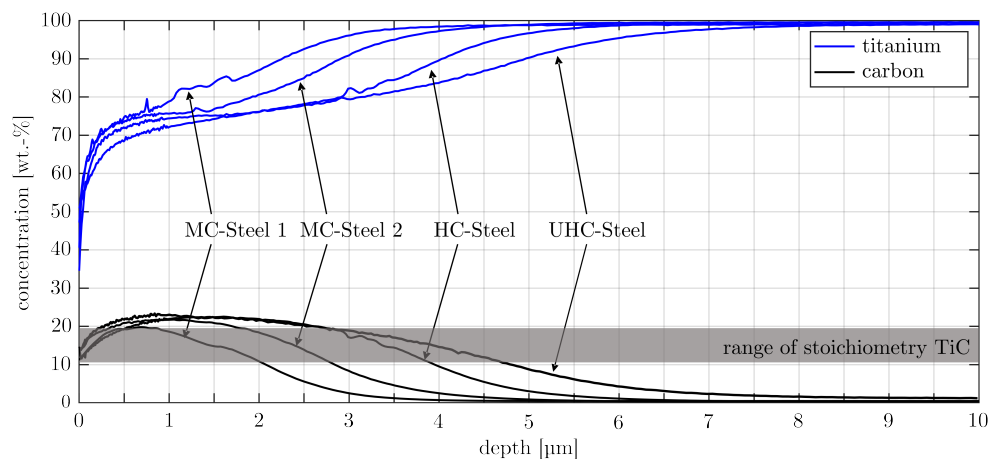


Figure 5. Quantified element depth profiles (in wt.-%) of the compound layer exposed by citric acid on the titanium substrate when using different carbon steels for hot pressing.

The penetration depth of the Cu-K α radiation is greater than the layer thickness, meaning that the basic substrate titanium is also measured. This correlation has been described in more detail in previous investigations [10]. Individual peaks could not be assigned to Ti or TiC. The peak at approx. $2\theta \approx 34^{\circ}$ matches the WL peak α -Ti (002) at $2\theta = 35.094^{\circ}$. The peak at $2\theta \approx 57^{\circ}$ corresponds to the WL peak of TiC (220) at $2\theta = 60.489^{\circ}$ and the peak at approx. $2\theta \approx 96^{\circ}$ corresponds to the WL peak of TiC (331) at $2\theta = 101.836^{\circ}$. The peak at approx. $2\theta \approx 45^{\circ}$ is assigned to the crystal orientation α -Fe (110) at $2\theta = 44.674^{\circ}$ in PDF-00-006-0696. When the steel was chemically removed using citric acid, some Fe traces remained on the surface. Apart from these peaks, no further peaks could be identified, which means that no other phases could be detected.

Some high-resolution EBSD images of the diffusion layer of a titanium–steel compound are shown in Figure 7. As shown in Figure 7a–c, the layer thickness increases with a rising carbon content of the steel. The microstructure shows a gradient structure. During high-temperature annealing, carbon atoms diffuse from the carbon steel into the Ti substrate. When the carbon concentration is supersaturated, TiC grains nucleate and grow. The TiC grain size is influenced by the nucleation density, which is initially high due to the high carbon concentration at the interface, resulting in a dense layer of fine TiC particles near the

surface. As the TiC layer grows inwards, the carbon concentration at the TiC/Ti interface decreases due to diffusion and carbon consumption during TiC precipitation, reducing the nucleation density and increasing the TiC grain size [7]. A large grain size of around $5\ \mu\text{m}$ is present towards the titanium base substrate, which Bai et al. [52] considered to be a high-quality metallurgical compound. In the top zone (left side of the respective cross-section), the grains are arranged in an equiaxed structure with a mean diameter of $d_G = 0.2\ \mu\text{m}$. The TiC grain size of the gradient structure varies in the range of $d_G = 0.15\text{--}4\ \mu\text{m}$. Its probability shows a lognormal distribution—see Figure 7d—with the maximum probability at a grain diameter of $d_G = 0.2\ \mu\text{m}$. The distribution is independent of the use of carbon steel. As the inverse pole figures of TiC in Figure 7a–c show, the crystallographic orientation of TiC is randomly distributed [10].

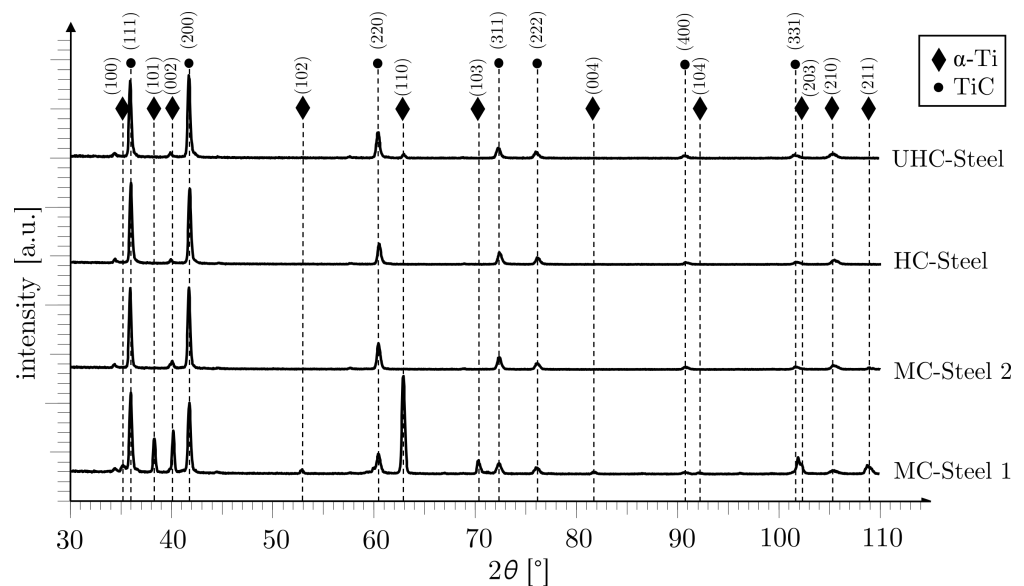


Figure 6. X-ray diffractograms of the compound layer (in diffusion direction) on the titanium substrate when using different carbon steels for hot pressing at $\vartheta = 950\ ^\circ\text{C}$ for $t_h = 4\ \text{h}$ and after the subsequent chemical removal of the carbon steel.

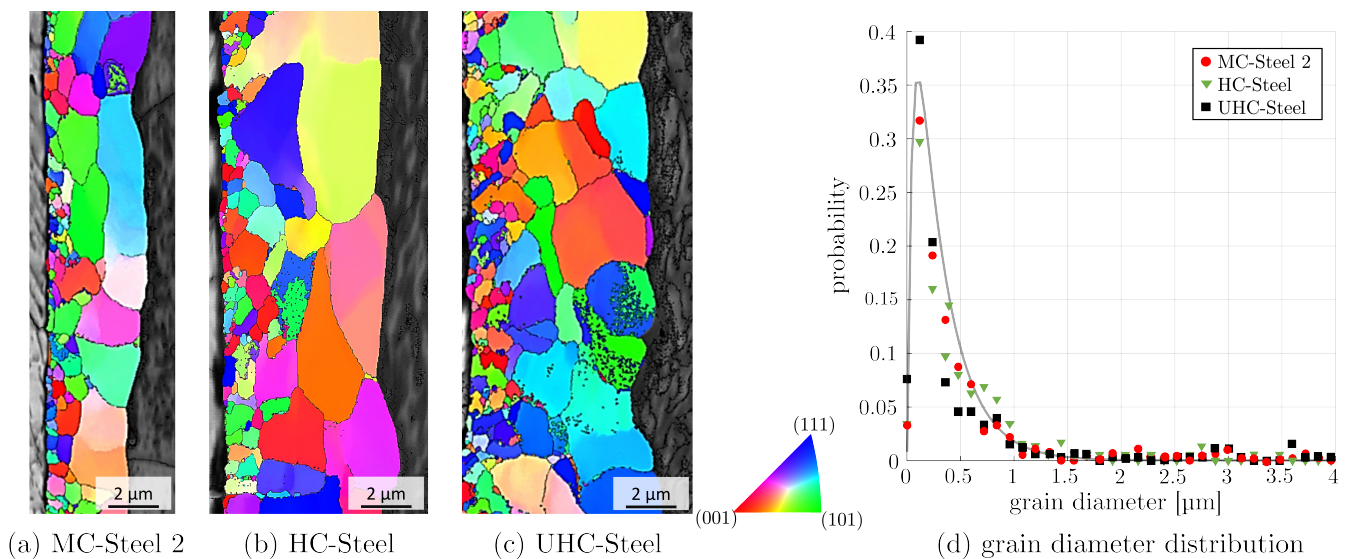


Figure 7. (a–c) Inverse pole figures from electron backscattered diffraction for diffusion direction using the different carbon steels as starting materials for hot pressing and (d) the probability distribution of grain size in the microstructure of the TiC layer.

The load–depth curves for the nanoindentation measurements are shown in Figure 8. At a maximum load of 50 mN, the indentation depth reached approximately 300 nm. Upon removal of the indenter, the sample recovered approx. 150 nm of this depth, indicating an elastic recovery of around 50%. The load–depth curve highlights the elastic–plastic deformation behavior under the nanoindenter’s influence. The corresponding hardness and elastic modulus values were determined to be $H = 35$ GPa and $E = 500$ GPa, respectively. These values are consistent with previous measurements using spheroidal cast iron as a carbon source [53]. Luo et al. have calculated a plasticity of 32% (68% elastic recovery) using nanoindentation measurements, indicating excellent mechanical properties [54]. They used C_2H_2 gas to produce a TiC layer with a porosity of nearly 24%. Mahmoodian et al. [55] determine a hardness of $H = 33.8$ – 36.6 GPa for a TiC layer produced by plasma. Zhao et al. [56] also measured a hardness of $H = 32$ GPa by hot pressing with needle cast iron. The Young’s modulus for stoichiometric TiC is described by Guemmaz et al. [27] as $E = 468$ GPa. The results of this investigation indicate that the hardness, Young’s modulus, and plasticity are comparable to the values measured in the literature. Table 3 summarizes the mechanical properties of the TiC layer, which indicate that these are independent of the steel used. Reference can also be made to the chemical composition (Figure 5) and the comparable microstructure (Figure 7) of the layer.

Table 3. Mechanical properties of the TiC layer formed at the interface of a titanium–steel bonding couple using different carbon steels as starting materials for hot pressing.

Carbon Steel	Hardness H [GPa]	Young’s Modulus E [GPa]	Elastic Recovery [%]
MC-Steel 2	(35.3 ± 3.3)	(515.2 ± 14.7)	(49.2 ± 3.4)
HC-Steel	(35.0 ± 3.2)	(509.8 ± 11.6)	(50.2 ± 2.7)
UHC-Steel	(35.2 ± 1.8)	(517.1 ± 29.0)	(48.9 ± 2.4)

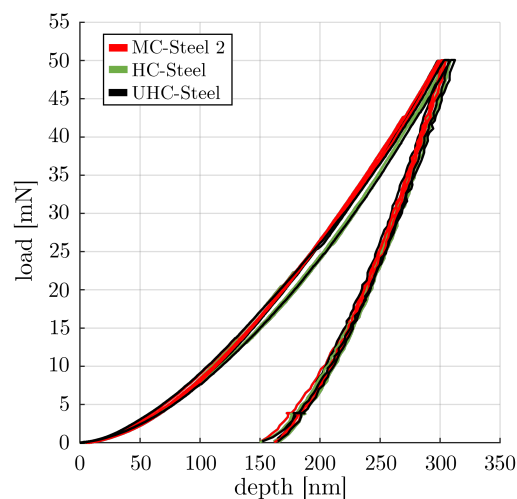


Figure 8. Nanoindentation measurements (load vs. depth) while using different carbon steels as starting materials for hot pressing.

4. Conclusions

The investigations confirm that it is possible to produce a dense and continuous TiC layer on a titanium substrate by hot pressing between titanium and carbon steels with varying carbon contents. The layer growth is diffusion-controlled and based on thermodynamic principles. The growth factor of the layer formation increases with the carbon content, while the activation energy remains almost constant. GDOES analyses confirm that the carbon content within the layer is independent of the steel used. This indicates that the layer is chemically saturated with carbon within the stoichiometric range of TiC, allowing this region to be etched by the Groesbeck etching solution. XRD

investigations confirm that no other intermetallic phases (FeTi or Fe₂Ti) are formed in addition to TiC. The layer exhibits a graded microstructure, which can be verified by EBSD measurements. This graded microstructure has no measurable impact on the mechanical properties of the layer.

The following conclusions can be drawn based on the present investigation:

1. **Influence of Carbon Content on Layer Thickness:** In addition to annealing temperature and time, the carbon content of the steel also affects the layer thickness. A maximum layer thickness of $d_L = 9.56 \mu\text{m}$ was achieved at $\vartheta = 1050 \text{ }^\circ\text{C}$ with an annealing time of $t_h = 4 \text{ h}$ using UHC steel (1.15 wt.-% C). The calculated activation energy of $Q = 126.5\text{--}136.7 \text{ kJ mol}^{-1}$ is independent of the carbon content in the steel. The layer growth of TiC is controlled by the reaction rate between titanium and carbon. The activation energy then relates to the reaction of C and Ti to TiC, which is not influenced by the carbon content of the steel, as the reaction is limited by the diffusion of C through TiC in Ti;
2. **Statistical Analysis of Layer Thickness:** Statistical analysis using ANOVA shows that the carbon content of the steel has the greatest influence on layer thickness. The other parameters (annealing time and process time) are also significant, but the carbon content has the most substantial impact on layer thickness;
3. **Carbon Distribution within the Layer:** The element distribution within the layer shows a graded carbon profile. The maximum carbon concentration is independent of the steel used; however, with higher carbon content in the steel, the maximum carbon concentration can be detected more deeply within the layer;
4. **X-ray Diffraction Analysis:** XRD analysis shows peaks only for α -Ti and TiC. As the layer thickens, the α -Ti peaks from the titanium substrate decrease, reflecting the penetration depth of the X-rays.
5. **Microstructure of the Layer:** The microstructure of the layer exhibits a graded grain size distribution, ranging from $d_G = 0.2 \mu\text{m}$ to $d_G = 5 \mu\text{m}$. The grain size distribution is independent of the steel's carbon content;
6. **Mechanical Properties and Carbon Content:** The layer exhibits a hardness of $H = 35 \text{ GPa}$, a Young's modulus of $E = 500 \text{ GPa}$, and nearly 50% elastic recovery after indentation. No correlation was observed between the mechanical properties of the layer and the carbon content of the steel. The observed stability in mechanical properties despite varying carbon contents in the starting steel can be explained by two main factors. First, the chemical composition of the TiC layer remains constant because it achieves a saturated carbon concentration that is independent of the carbon content in the starting steel. As a result, variations in the steel's carbon content do not affect the layer's chemical composition. Second, the microstructure of the TiC layer remains consistent across different steel carbon contents, showing no significant differences. This uniform microstructure indicates that the mechanical properties of the TiC layer are unaffected by the carbon content of the steel.

The results indicate that the TiC layer produced by hot pressing is stable and mechanically effective, regardless of the carbon content of the steel. The primary factors affecting the properties of the layer are the processing conditions, such as temperature and time, as well as the chemical composition of the layer itself. The carbon content of the steel does not significantly impact the mechanical properties of the TiC layer.

Author Contributions: Conceptualization, M.G. and L.S.; methodology, M.G., J.Z. and U.S.; software, J.Z. and A.D.; validation, M.G., A.D., U.S. and L.S.; formal analysis, L.E. and U.S.; investigation, M.G., A.D. and L.S.; resources, A.D. and L.S.; data curation, U.S. and J.Z.; writing—original draft preparation, M.G., J.Z. and L.S.; writing—review and editing, M.G., L.E. and U.N.; visualization, L.E. and J.Z.; supervision, U.N. and L.S.; project administration, U.N.; funding acquisition, M.G. and U.N. All authors have read and agreed to the published version of the manuscript.

Funding: The publication of this article was funded by the Open Access Publishing Fund of OTH Regensburg.

Data Availability Statement: All the relevant data are included within the manuscript. The data presented in this study are available on request from the corresponding author.

Acknowledgments: Thanks to the Thüringer Graduiertenförderung for the financial support provided to M. Grad.

Conflicts of Interest: The authors declare no conflicts of interest. The funders had no role in the design of the study; in the collection, analyses, or interpretation of data; in the writing of the manuscript; or in the decision to publish the results.

Abbreviations

The following abbreviations are used in this manuscript:

XRD	X-ray Diffraction
EBS	Electron Backscatter Diffraction
GDOES	Glow Discharge Optical Emission Spectroscopy
OM	Optical Microscope
ANOVA	Analysis of Variance
RSM	Response Surface Methodology
LC-Steel	Low-Carbon Steel
MC-Steel	Medium-Carbon Steel
HC-Steel	High-Carbon Steel
UHC-Steel	Ultra-High-Carbon Steel
SEM	Scanning Electron Microscope

Appendix A

Table A1. Analysis of variance (ANOVA) of the RSM model corresponding to the response: layer thickness.

Source	DF	Adj SS	Adj MS	F-Value	p-Value
layer thickness	9	111.083	12.3425	166.19	0.000
Linear	3	108.376	36.1252	486.41	0.000
carbon content	1	50.777	50.7775	683.70	0.000
temperature	1	37.715	37.7147	507.83	0.000
annealing time	1	19.359	19.3590	260.66	0.000
Square	3	1.362	0.4541	6.11	0.003
carbon content × carbon content	1	0.103	0.103	1.39	0.250
temperature × temperature	1	0.055	0.055	0.74	0.397
annealing time × annealing time	1	1.204	1.2044	16.22	0.000
2-Way Interaction	3	2.442	0.8138	10.96	0.000
carbon content × temperature	1	1.292	1.2917	17.39	0.000
carbon content × annealing time	1	0.087	0.0873	1.18	0.288
temperature × annealing time	1	1.062	1.0625	14.31	0.001
Error	26	1.931	0.0743		
Total	35	113.014			

DF = Degree of Freedom; Adj SS = Adjusted sums of squares; Adj MS = Adjusted mean squares; F-Value = Variance; p-Value = test statistic.

References

- Duan, H.q.; Han, Y.f.; Lü, W.j.; Mao, J.w.; Wang, L.q.; Zhang, D. Effect of solid carburization on surface microstructure and hardness of Ti-6Al-4V alloy and (TiB+La₂O₃)/Ti-6Al-4V composite. *Trans. Nonferrous Met. Soc. China* **2016**, *26*, 1871–1877. [\[CrossRef\]](#)
- Bailey, R.; Sun, Y. Pack carburisation of commercially pure titanium with limited oxygen diffusion for improved tribological properties. *Surf. Coatings Technol.* **2015**, *261*, 28–34. [\[CrossRef\]](#)
- Nishimoto, A.; Nishi, C. Carbide layer coating on titanium by spark plasma sintering technique. *Surf. Coatings Technol.* **2018**, *353*, 324–328. [\[CrossRef\]](#)
- Geetha, M.; Singh, A.K.; Asokamani, R.; Gogia, A.K. Ti based biomaterials, the ultimate choice for orthopaedic implants—A review. *Prog. Mater. Sci.* **2009**, *54*, 397–425. [\[CrossRef\]](#)

5. Lohse, B.H.; Calka, A.; Wexler, D. Effect of starting composition on the synthesis of nanocrystalline TiC during milling of titanium and carbon. *J. Alloys Compd.* **2005**, *394*, 148–151. [[CrossRef](#)]
6. Seifert, H.J.; Lukas, H.L.; Petzow, G. Thermodynamic optimization of the Ti-C system. *J. Phase Equilibria* **1996**, *17*, 24–35. [[CrossRef](#)]
7. Zhao, Z.; Hui, P.; Wang, T.; Wang, X.; Xu, Y.; Zhong, L.; Zhao, M. New strategy to grow TiC coatings on titanium alloy: Contact solid carburization by cast iron. *J. Alloys Compd.* **2018**, *745*, 637–643. [[CrossRef](#)]
8. Li, B.; Chen, Z.; He, W.; Zhou, T.; Wang, Y.; Peng, L.; Li, J.; Liu, Q. Effect of titanium grain orientation on the growth of compounds at diffusion bonded titanium/steel interfaces. *Mater. Charact.* **2019**, *148*, 243–251. [[CrossRef](#)]
9. Zhao, Z.; Hui, P.; Liu, F.; Zhong, L.; Zhao, M.; Li, B.; Yan, F.; Lu, Z.; Ding, Y.; Xu, Y. A key to tune the grain size gradient of the TiC coating on titanium by interstitial carburization: The timing for pressing. *J. Alloys Compd.* **2020**, *817*, 152725. [[CrossRef](#)]
10. Grad, M.; Honig, H.; Diemar, A.; Flock, D.; Spieß, L. Complex material analysis of a TiC coating produced by hot pressing with optical light microscopy, EDS, XRD, GDOES and EBSD. *Surf. Coatings Technol.* **2024**, *476*, 130265. [[CrossRef](#)]
11. Yu, C.; Fu, L.; Xiao, H.; Lv, Q.; Gao, B. Effect of carbon content on the microstructure and bonding properties of hot-rolling pure titanium clad carbon steel plates. *Mater. Sci. Eng. A* **2021**, *820*, 141572. [[CrossRef](#)]
12. Momono, T.; Enjo, T.; Ikeuchi, K. Effects of Carbon Content on the Diffusion Bonding of Iron and Steel to Titanium (Momono, 1990). *Isij Int.* **1990**, *30*, 978–984. [[CrossRef](#)]
13. Hayashi, T.; Matsuura, K.; Ohno, M. TiC Coating on Titanium by Carbonization Reaction Using Spark Plasma Sintering. *Mater. Trans.* **2013**, *54*, 2098–2101. [[CrossRef](#)]
14. Zhao, Z.; Hui, P.; Liu, F.; Wang, X.; Li, B.; Xu, Y.; Zhong, L.; Zhao, M. Fabrication of TaC coating on tantalum by interstitial carburization. *J. Alloys Compd.* **2019**, *790*, 189–196. [[CrossRef](#)]
15. Liu, H.; Zhang, X.; Jiang, Y.; Zhou, R. Microstructure and high temperature oxidation resistance of in-situ synthesized TiN/Ti3Al intermetallic composite coatings on Ti6Al4V alloy by laser cladding process. *J. Alloys Compd.* **2016**, *670*, 268–274. [[CrossRef](#)]
16. Algodí, S.J.; Murray, J.W.; Fay, M.W.; Clare, A.T.; Brown, P.D. Electrical discharge coating of nanostructured TiC-Fe cermets on 304 stainless steel. *Surf. Coatings Technol.* **2016**, *307*, 639–649. [[CrossRef](#)]
17. Friedrich, R.; Holger, F.; Jens, B. ThermoOptische Messverfahren (TOM) für die Hochtemperatur-Prüfung von Feuerfestwerkstoffen. *Prozesswärme* **2019**, *1/2019*, 63–68.
18. He, P.; Feng, J.; Zhang, B.; Qian, Y. Microstructure and strength of diffusion-bonded joints of TiAl base alloy to steel. *Mater. Charact.* **2002**, *48*, 401–406. [[CrossRef](#)]
19. Candioti, L.V.; de Zan, M.M.; Cámara, M.S.; Goicoechea, H.C. Experimental design and multiple response optimization. Using the desirability function in analytical methods development. *Talanta* **2014**, *124*, 123–138. [[CrossRef](#)]
20. Spieß, L.; Teichert, G.; Schwarzer, R.; Behnken, H.; Genzel, C. *Moderne Röntgenbeugung-Röntgendiffraktometrie für Materialwissenschaftler, Physiker und Chemiker*, 3rd ed.; Springer: Berlin/Heidelberg, Germany, 2019; p. 635. [[CrossRef](#)]
21. Dinnebier, R.E.; Billinge, S. *Rietveld Refinement—Practical Powder Diffraction Pattern Analysis Using Topas*, 1st ed.; De Gruyter: Berlin, Germany
22. Souza, J.G.S.; Cordeiro, J.M.; Lima, C.V.; Barão, V.A.R. Citric acid reduces oral biofilm and influences the electrochemical behavior of titanium: An in situ and in vitro study. *J. Periodontol.* **2019**, *90*, 149–158. [[CrossRef](#)]
23. Grimm, W. Eine neue Glimmentladungslampe für die optische Emissionsspektalanalyse. *Spectrochim. Acta Part B At. Spectrosc.* **1968**, *23*, 443–454. [[CrossRef](#)]
24. Fundenberger, J.-J.; Beausir, B. *Analysis Tools for Electron and X-ray Diffraction*; Université de Lorraine-Metz: Metz, France, 2017.
25. Oliver, W.C.; Pharr, G.M. An improved technique for determining hardness and elastic modulus using load and displacement sensing indentation experiments. *J. Mater. Res.* **1992**, *7*, 1564–1583. [[CrossRef](#)]
26. Kvashina, T.; Uvarov, N.; Ukhina, A. Synthesis of Titanium Carbide by Means of Pressureless Sintering. *Ceramics* **2020**, *3*, 306–311. [[CrossRef](#)]
27. Guemmaz, M.; Mosser, A.; Boudoukha, L.; Grob, J.J.; Raiser, D.; Sens, J.C. Ion beam synthesis of non-stoichiometric titanium carbide: Composition structure and nanoindentation studies. *Nucl. Instruments Methods Phys. Res. Sect. B Beam Interact. Mater. Atoms* **1996**, *111*, 263–270. [[CrossRef](#)]
28. Hainsworth, S.V.; Page, T.F. Evaluation of the mechanical properties of ceramics and thin hard ceramic coatings using nanoindentation *Nondestruct. Test. Eval.* **2001**, *4–5*, 275–298. [[CrossRef](#)]
29. Wang, H.; Huang, Z.; Lu, Z.; Wang, Q.; Jiang, J. Determination of the elastic and plastic deformation behaviors of Yb:Y3Al5O12 transparent ceramic by nanoindentation. *J. Alloys Compd.* **2016**, *682*, 35–41. [[CrossRef](#)]
30. Luo, Y.; Jiang, H.; Cheng, G.; Liu, H. Effect of carburization on the mechanical properties of biomedical grade titanium alloys. *J. Bionic Eng.* **2011**, *8*, 86–89. [[CrossRef](#)]
31. Fischer-Cripps, A.C. Nanoindentation In *Springer—Mechanical Engineering Series*, 2nd ed.; Springer: New York, NY, USA, 2004. [[CrossRef](#)]
32. Kim, Y.J.; Chung, H.; Kang, S.J. In situ formation of titanium carbide in titanium powder compacts by gas–solid reaction. *Compos. Part A Appl. Sci. Manuf.* **2001**, *32*, 731–738. [[CrossRef](#)]
33. Arvieu, C.; Manaud, J.P.; Quenisset, J.M. Interaction between titanium and carbon at moderate temperatures. *J. Alloys Compd.* **2004**, *368*, 116–122. [[CrossRef](#)]

34. Bucur, E.; Wagner, F.C. *Rate of Diffusion of Carbon in Alpha and in Beta Titanium as a Function of the Temperature and Concentration*; Defense Technical Information Center: Fort Belvoir, VA, USA, 1954. [[CrossRef](#)]
35. Capaldi, M.J.; Saidi, A.; Wood, J.V. Reaction Synthesis of TiC and Fe-TiC Composites. *ISIJ Int.* **1997**, *37*, 188–193. [[CrossRef](#)]
36. Feng, Z.; Duan, Y.; Peng, M. Growth Kinetics, and Wear and Corrosion Properties of TiC Coatings on Pure Titanium by Carburizing. *Metall. Mater. Trans. A* **2023**, *54*, 2947–2959. [[CrossRef](#)]
37. Khataee, A.R.; Kasirib, M.B.; Alidokht, L. Application of response surface methodology in the optimization of photocatalytic removal of environmental pollutants using nanocatalysts. *Environ. Technol.* **2011**, *33*, 1669–1684. [[CrossRef](#)] [[PubMed](#)]
38. Liu, W.; DuPont, J.N. Fabrication of functionally graded TiC/Ti composites by Laser Engineered Net Shaping. *Scr. Mater.* **2003**, *48*, 1337–1342. [[CrossRef](#)]
39. Chaus, A.S.; Rudnickii, F.I. Diffusion and Secondary Carbide Precipitation in High-Speed Steels. *Defect Diffus. Forum* **2010**, *297–301*, 1071–1076. [[CrossRef](#)]
40. Kaya, M.; Kılıç, M.; Kırık, İ.; Karakurt, E.M.; Gülenç, B. Diffusion bonding between Ti-6Al-4V alloy and interstitial free steel. *Mater. Und Werkst.* **2017**, *48*, 661–665. [[CrossRef](#)]
41. Kundu, S.; Chatterjee, S. Diffusion bonding between commercially pure titanium and micro-duplex stainless steel. *Mater. Sci. Eng. A* **2008**, *480*, 316–322. [[CrossRef](#)]
42. Kurt, B.; Orhan, N.; Evin, E.; Çalik, A. Diffusion bonding between Ti-6Al-4V alloy and ferritic stainless steel. *Mater. Lett.* **2007**, *61*, 1747–1750. [[CrossRef](#)]
43. Yang, X.; Guo, K.; Gao, Y.; Wu, B.; Li, J.; Gao, Y.; Wang, Q.; Zhang, F. Effect of carbon content on interfacial microstructure and mechanical properties of a vacuum hot-compressed bonding titanium-steel composite. *Mater. Sci. Eng. A* **2021**, *824*, 141802. [[CrossRef](#)]
44. Chiba, A.; Nishida, M.; Morizono, Y.; Imamura, K. Bonding characteristics and diffusion barrier effect of the TiC phase formed at the bonding interface in an explosively welded titanium/high-carbon steel clad. *J. Phase Equilibria* **1995**, *16*, 411–415. [[CrossRef](#)]
45. Chai, X.Y.; Chen, G.; Chai, F.; Pan, T.; Yang, Z.G.; Yang, C.F. Hot roll bonding between commercially pure titanium and high-strength low-alloy steel using Fe interlayer. *J. Iron Steel Res. Int.* **2019**, *26*, 1126–1136. [[CrossRef](#)]
46. Yu, C.; Qi, Z.c.; Yu, H.; Xu, C.; Xiao, H. Microstructural and Mechanical Properties of Hot Roll Bonded Titanium Alloy/Low Carbon Steel Plate. *J. Mater. Eng. Perform.* **2018**, *27*, 1664–1672. [[CrossRef](#)]
47. Walser, R.M.; Bené, R.W. First phase nucleation in silicon-transition-metal planar interfaces. *Appl. Phys. Lett.* **1976**, *28*, 624–625. [[CrossRef](#)]
48. Murray, J.L. (Ed.) *Phase Diagrams of Binary Titanium Alloys*, 2nd ed.; Monograph Series on Alloy Phase Diagrams; ASM Internat: Metals Park, OH, USA, 1990; Volume 2.
49. Massalski, T.B.; Murray, J.L.; Bennett, L.H.; Baker, H. *Binary Alloy Phase Diagrams*, 2nd ed.; American Society for Metals: Metals Park, OH, USA, 1987.
50. Gusev, A.I. (Ed.) *Phase Equilibria, Phases and Compounds in the Ti-C System*; Elsevier: Amsterdam, The Netherlands, 2002.
51. Kocuyigit, M.; Camurlu, H.E. Volume Combustion Synthesis in Fe-Ti-C and Fe-Ti Systems. *Metall. Mater. Trans. A* **2023**, *54*, 320–332. [[CrossRef](#)]
52. Bai, H.; Zhong, L.; Shang, Z.; Xu, Y.; Wu, H.; Bai, J.; Ding, Y. Microstructure and mechanical properties of TiC-Fe surface gradient coating on a pure titanium substrate prepared in situ. *J. Alloys Compd.* **2019**, *771*, 406–417. [[CrossRef](#)]
53. Grad, M.; Nadammal, N.; Tytco, D.; Noster, U. On the nanoindentation behavior of a TiC layer formed through thermo-reactive diffusion during hot pressing of Ti and cast iron. *Mater. Lett. X* **2022**, *15*, 100161. [[CrossRef](#)]
54. Luo, Y.; Ge, S.; Zhang, D.; Wang, Q.; Liu, H. Fretting wear of carburized titanium alloy against ZrO₂ under serum lubrication. *Tribol. Int.* **2011**, *44*, 1471–1475. [[CrossRef](#)]
55. Mahmoodian, R.; Hamdi, M.; Hassan, M.A.; Akbari, A. Mechanical and Chemical Characterization of a TiC/C System Synthesized Using a Focus Plasma Arc. *PLoS ONE* **2015**, *10*, e0130836. [[CrossRef](#)] [[PubMed](#)]
56. Zhao, B.; Jian, D.; Ma, L.; Ding, Y.; Zhou, L. Precipitation of intermetallic compounds in brazing of titanium and steel using brass filler. *J. Mater. Process. Technol.* **2020**, *285*, 116730. [[CrossRef](#)]

Disclaimer/Publisher's Note: The statements, opinions and data contained in all publications are solely those of the individual author(s) and contributor(s) and not of MDPI and/or the editor(s). MDPI and/or the editor(s) disclaim responsibility for any injury to people or property resulting from any ideas, methods, instructions or products referred to in the content.